

USING BOUNDARY ELEMENT MODELING OF FAULT SLIP TO PREDICT PATTERNS OF STRESS PERTURBATION AND RELATED FRACTURES IN GEOTHERMAL RESERVOIRS AND EXPLORE PARAMETER UNCERTAINTY

Michael W. Swyer and Nicholas C. Davatzes

Temple University
1901 n. 13th Street
Earth and Environmental Science, Beury Hall, Rm. 307
Philadelphia, PA, 19122
e-mail: Michael.Swyer@temple.edu, Davatzes@temple.edu

ABSTRACT

Geologic structures at the surface such as fault tips, intersections, and fault relays are known to concentrate stress that can promote increased fracture density or reactivation in response to fault slip that facilitate fluid flow. The stress state driving slip determines where along the fault slip occurs that will induce deformation in the adjacent rock volume to promote or inhibit fracture formation or reactivation. Unfortunately, both the geometry and stress state have significant uncertainties that will impact the usefulness of this information in prospecting for geothermal resources, developing a reservoir model, distinguishing between competing models, or quantifying the probability of model validity. The impact of these uncertainties on the reservoir model can be quantitatively evaluated through efficient numerical modeling that iteratively explores the range of uncertainty in the controlling parameter space. The boundary element method is used to model fault slip (or opening) and calculate stress/strain variation.

The Rhyolite Ridge fault system located at the Desert Peak Geothermal Field in Nevada is modeled in this study as an example of a blind geothermal field associated with a geometrically complex fault, which is poorly constrained at depth. We explore the impact of that uncertainty to better constrain the fault geometry at depth, evaluate the impact of uncertainty in tectonic stresses predictions of deformation, and thus the predicted pattern of fracture slip and formation. We find that the level of uncertainty in fault geometry leads to a high degree of variability in the locations experiencing stress states that promote fracture. But for instance, only a narrow subset of fault heights and dips approach the observed stress state in well DP27-15. In addition, the most stable stress concentrations occur within

relays between unconnected fault segments.

INTRODUCTION

In many cases, geothermal systems in the Basin and Range tectonic province have no surface expression that reveals the resource or that can guide the development of reservoirs. Even in developed reservoirs, key information about the subsurface structure controlling heat/fluid flow can be missing. Determining zones ideal for geothermal production can thus be difficult in the absence of hot springs at the surface, or thermal anomalies either evident at the surface (e.g., Coolbaugh et al., 2007) or from existing boreholes. In addition, these approaches to geothermal exploration and development of reservoir models are costly and time consuming, and do not guarantee a well-constrained reservoir model, or a viable reservoir at all.

The subsurface model of the reservoir depends strongly on faults and fracture systems which are known to act as fluid conduits that host deep circulation of water and contribute to reservoir storativity (Smith et al., 1990; Bruhn et al., 1994; Barton et al., 1995; Cain et al., 1996; Curewitz and Karson, 1997; Fairley and Hinds, 2004). In the Basin and Range, many hydrothermal systems are controlled by the active, extensional normal faults characteristic of the region that provide the vertically extensive conduits necessary to bring hot water to shallow depth by groundwater circulation (e.g., Barton et al., 1998; Hickman et al., 1998). Nevertheless, the site of hydrothermal upwelling shows a complex relationship to these faults, with resources localized along limited portions of the faults, at fault bends and terminations (tips), or in regions of fault intersection or overlap (Curewitz and Karson, 1997; Hickman et al., 1998; Eichhubl et al., 2009; Faulds et al., 2004). Virtually all fault systems contain complex geometry of this nature but only few

maintain permeability over long periods of time.

Our conceptual model is that these large faults deform the adjacent volume of rock to produce fractures and maintain open fracture networks that provide the necessary conduits for fluid flow as well as sufficient storativity and heat exchange area to support geothermal production. The complex fault geometry in a geothermal field can serve to concentrate stress and promote increased fracture density that is conducive of fluid flow and heat extraction (Curewitz and Karson, 1997; Maerten et al., 1999; Bourn et al., 2001; Mickelthwaite et al., 2009). Slip along the fault(s) is driven by the local stress and can lead to complicated patterns of deformation, i.e. shear slip and dilation within the surrounding protolith. (e.g., Bourn et al., 2001; Davatzes et al., 2005; Mickelthwaite et al., 2009). The resulting damage zone should reflect the pattern of stress change accompanying slip on geometrically complex fault systems, therefore defining the limited portions of faults that might support the deep circulation necessary to support a geothermal reservoir.

The Desert Peak Geothermal Field, NV, is one example of a hydrothermal area associated with a bend or step in the Rhyolite Ridge normal fault system (Figure 1a). Enhanced Geothermal System (EGS) well DP 27-15 is located along the northernmost N-NE striking fault trace with active injecting and producing wells located within ~0.5 to ~2 km to the SW along the fault strike, and just beyond the apparent tip of the fault or within an extensional step or bend (Figure 1b). Although this spatial association is clear, several problems remain: (1) The fault is comprised of several distinct segments, making it uncertain whether all, some, or none are actively slipping; (2) Stress transfer among segments can produce spatially varying patterns of slip direction on the fault segments and deformation in the surrounding volume; (3) All of the key parameters including the fault geometry, mechanical properties of the rock, and the stress state have associated uncertainties, especially at depth.

We investigate the structural control of the Rhyolite Ridge fault system on fracture potential, i.e., the conditions promoting fracture formation and slip at Desert Peak through boundary element modeling (BEM) of slip on the Rhyolite Ridge fault system and resulting deformation in the adjacent rock volume. A heuristic modeling approach is adopted to investigate the sensitivity of this elastic deformation to details of fault geometry and stress state within uncertainties derived from mapping and borehole studies as well as reasonable constraints on the state of stress in the surrounding crustal volume from the frictional strength of rock. Variation in the outcomes of these

models can be quantified by exploring these uncertainties, thus revealing which results are poorly constrained due to the uncertainty of input model parameters and which outcomes are robust and have a high probability of occurrence. We show that this approach provides a practical tool for geothermal exploration and development by 1) determining which geologic models are compatible with field observations and 2) identifying the types of data and locations that would be most useful to refine or test a geologic model.

GEOLOGIC SETTING

The Desert Peak Geothermal Field is located in the Basin and Range Tectonic Province along the N-NE striking Rhyolite Ridge normal fault system. The Rhyolite Ridge Fault System is characterized by multiple fault segments with abundant bends and intersections near the production wells. The hydrothermal system itself has no active surface expression that would indicate the presence of a geothermal reservoir (Figure 1b) (Benoit et al., 2006; Kratt et al., 2006; Faulds and Garside, 2003).

Several geothermal systems including Dixie Valley, Fallon, Desert Queen, and Brady's among others are similarly associated with N-NE striking normal fault systems. The adjacent Brady's Geothermal Field has a high fault density and surface expression in the form of hot springs and hydrothermal silica deposits (Kratt, et al., 2006) (Figure 1a). Desert Peak is also near the Desert Queen Geothermal Field that has been shown to have a thermal anomaly through shallow temperature probe profiling that coincides with a densely faulted area (Coolbaugh et al. 2007; Faulds and Garside, 2003), but which is not yet developed.

The conceptual fault model for Rhyolite Ridge is that two major N-NE striking faults have formed an active left-stepping overlapping relay that has been breached through fault tip propagation and truncating intersections (Faulds and Garside, 2003), thus hard-linking the relay. Slip on these segments could cause stress concentrations that increase fracture density. The characteristics of the system are derived from surface fault maps (e.g., Faulds and Garside, 2003; Faulds pers comm. November, 2011), geological characterization of well data (Lutz et al., 2009), geomechanical analysis of well data (Robertson-Tait et al., 2004; Davatzes and Hickman, 2009; Hickman and Davatzes, 2010), and rock mechanical analysis of representative core (Lutz et al., 2010). Additional constraints on the behavior of the reservoir are derived from pressure interference tests (Zemach et

al., 2010), tracer studies (Rose et al., 2010), and local seismic monitoring (see Nathwani et al., 2011).

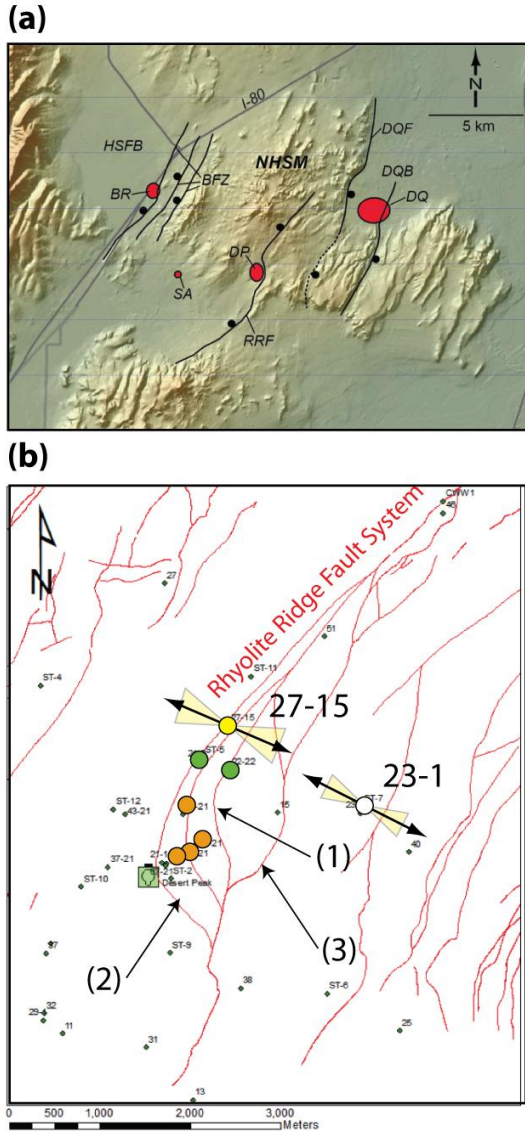


Figure 1: Desert Peak-Bradys-Desert Queen Geothermal fields. (a) Fault systems and associated thermal anomalies for the three geothermal fields (figure reproduced from Faulds et al., 2010) (b) Rhyolite Ridge fault system at Desert Peak, Shmin orientations for wells DP 27-15 and DP 23-1, and fault relay traces modeled.

METHODOLOGY

The numerical modeling method used in this study is the linear elastic boundary element method (Crouch and Starfield, 1983) implemented in the Poly3D (Thomas, 1992) modeling software. In Poly3D, the fault surfaces are discretized into triangular elements modeled as displacement

discontinuities within a continuous isotropic homogeneous linear elastic half or whole space rather than discretizing the entire three-dimensional rock volume, resulting in much more efficient computation. Temperature, fluid flow, or chemical effects are not modeled. Displacement discontinuity or traction boundary conditions are specified on the elements and a uniform far field strain or stress tensor is applied to induce deformation. A quasi-static solution of stress and strain is calculated at observation points in the surrounding volume using linear elastic properties (Figure 2). In this initial series of models, the elements comprising the faults were specified to have zero residual shear tractions and zero normal displacement – effectively simulating a complete shear stress drop without opening or interpenetration of the modeled surfaces. The uniform remote stress tensor is consistent with the approximate reservoir depth of 930 m (Table 1).

The efficiency of the BEM allows us to investigate the sensitivity of the computed stress/strain or fault slip distribution to various modeling parameters by systematically sampling them within the range of uncertainty. Multiple modeling parameters may be sampled together to explore a parameter space that quantifies trade-offs in the model response of closely related properties.

Model calibration is achieved by comparing the model results to observation points placed coinciding with well DP 23-1, which has been logged to determine the direction of the principal horizontal stresses (Robertson-Tait et al., 2004), and well DP 27-15, for which the direction and magnitude of the least compressive horizontal stress, Shmin, has been determined (Davatzes and Hickman, 2009; Hickman and Davatzes, 2010) (Figure 1b). The fracture populations intersecting both wells have also been determined through analysis of image logs.

The edges of boundary elements are associated with a stress singularity that roughly affects the volume within one element length. The balance between resolving physically realistic stress at short distances from the modeled fault and numerical efficiency resulting from fewer boundary elements was assessed by progressively reducing the element edge length and observing the state of stress at a position representing the DP 27-15 borehole. This position afforded both ready comparison to the stress tensor measured in the field (e.g., Hickman and Davatzes, 2010) and was at a distance that is short compared to the geometric complexity modeled later in this study. For simplicity, the model fault was taken as a rectangular flat plane representative of the northernmost fault trace of Rhyolite Ridge and assigned a dip of 60°, typical for normal faults. The stress tensor initially used is derived from the

magnitude and direction of S_{hmin} observed in well DP 27-15, the vertical stress, or SV, from the weight of the overlying rock, and the most compressive horizontal stress, or S_{Hmax} , assumed to be the average of the other two principal stresses (Figure 2) as described by Hickman and Davatzes (2010) (Table 1). The pore pressure, or PP, used was taken as hydrostatic pressure from the depth to the water table, and the elastic properties of Young's Modulus and Poisson's Ratio of the surrounding rock were taken from the results of triaxial compression tests of representative rock samples taken from borehole 35-13 (Lutz et al., 2010).

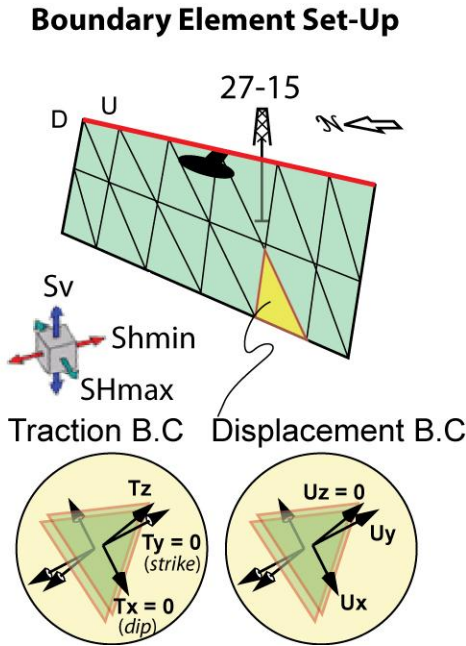


Figure 2: Model Setup for Rhyolite Ridge. Location of DP 27-15, remote stress tensor and boundary conditions

Using the same model configuration to test the element edge length, we determined the model is relatively insensitive to Poisson's Ratio and Young's Modulus within the range of uncertainty, so representative values from the laboratory tests of 34.2 GPa for Young's Modulus and 0.18 for Poisson's Ratio were used for all subsequent modeling.

Table 1: Model Parameters (individual models differ as stated)

| Parameter | Magnitude | Uncertainty Range | Units |
|-----------------------------|-----------|-------------------|---------|
| <i>Geometry¹</i> | | | |
| • Approx. element length | 200 | - | m |
| • Fault dip | 60 | ± 15 | degrees |
| • Depth to lower fault tip | 2000 | - | m |

| | | | |
|---------------------------------------|------|--------|----------|
| <i>Stress Model</i> | 930 | ± 12.5 | m |
| <i>Depth(DP27-15)²</i> | | | |
| • S_V | 22.6 | ± 0.7 | MPa |
| • S_{hmin} | 13.8 | ± 0.4 | MPa |
| • S_{Hmax} | 18.2 | ± 0.6 | MPa |
| • P_p | 8.0 | ± 0.6 | MPa |
| • S_{hmin} Azimuth | 114 | ± 17 | azimuth |
| <i>Elastic Properties³</i> | | | |
| • Young's Modulus, E | 34.2 | ± 11.0 | GPa |
| • Poisson's Ratio, ν | 0.18 | ± 0.07 | unitless |
| <i>Rock Properties³</i> | | | |
| • Laboratory Friction | 0.77 | ± 0.12 | unitless |

¹ Faults and Garside (2003); Faults pers. comm. November 2011

² Hickman and Davatzes (2010)

³ Lutz et al., (2010)

RESULTS

Modeling of the fault system at Desert Peak was conducted through various sensitivity studies of fault geometry and far-field stress state. (1) In the first series of models, the fault geometry was tested by varying fault dip and in-plane length from the surface to the lower tip of the fault along a flat planar rectangular fault (depth). (2) The remote stress tensor was varied by allowing a range from normal faulting to strike slip stress regimes. (3) The fault step along the Rhyolite Ridge system was modeled in two configurations: (a) as two independent segments in which the spacing of these segments was systematically varied and (b) as a continuous fault with a bend that reproduces the geometry of mapped fault segments.

(1) Simple Geometry Sensitivity Study

The dip angle and depth to the lower tip of the Rhyolite Ridge Fault systems are poorly constrained by outcrop (Faults and Garside, 2003), seismic reflection (Zemach et al., 2010), earthquake (e.g., Nathwani et al., 2011), and borehole data (Faults et al., 2003; Lutz et al., 2009). To constrain these geometric parameters, we model response to variations in fault dip and in-plane fault length perpendicular to strike (depth). The azimuth of the remote S_{hmin} (S_{hmin}^{rem}) was set perpendicular to the fault strike so that the fault orientation is reflective of remote stresses assumed to cause fault formation (Jaeger and Cook, 1979). The magnitude of S_{hmin}^{rem} was derived from a critically stressed friction failure criterion for normal faults (Jaeger and Cook, 1979; Zoback, 2007):

$$S_{hmin}^{rem} = \frac{S_v - P_p}{\left[(\mu^2 + 1)^{1/2} + \mu \right]} + P_p \quad \text{Eq. 1}$$

Where μ is the coefficient of friction, taken as 0.77 which is the value obtained from triaxial compression testing of rock samples from Desert Peak (Lutz et al., 2010). Since the model includes a complete stress drop, these results represent the maximum stress perturbation. The resulting stress distribution is calculated at the stimulation depth in well DP 27-15. The results of all analyses are contoured as a function of this parameter space (Figure 3). The model is very sensitive to changes in fault depths less than ~4000m, but was not sensitive to fault dip. The model is more sensitive to dip for fault depths greater than 6000 meters, but fault depths greater than this did not affect the model results. The magnitudes of locally induced S_{hmin} (S_{hmin}^{loc}) dropped below the boundary conditions at roughly 1000 meters of depth-extent, but became relatively more compressive at a depth of 2000 m, and showed the highest magnitude at this depth for steeply dipping faults (Figure 3a). Although none of the model results were as high as the observed S_{hmin}^{loc} magnitude of 13.8 MPa at ~930 m depth, the dip and depth combination of 71° and 2000 meters produced the most compressive value. The azimuth of 114 for S_{hmin}^{loc} observed in the well was also achieved at this depth (Figure 3b), as well as the value of S_v assumed to be 22.6 MPa from the weight of the rock overburden (Figure 3c).

Since drilling induced tensile fractures are parallel to the borehole axis within a 12-15 degree uncertainty (Davatzes and Hickman, 2009) and given the precision of the method to asses this orientation (Peška and Zoback, 1995), a key criterion for the suitability of the model is the variation of the maximum principal compressive stress from vertical. Therefore, S_v can be assumed to be a principal stress in the vertical direction from the well observation, however, the most compressive principal stress in the model was not vertical, implying that the principal stresses show significant rotation at this location due to slip. The magnitude of locally induced S_v can also diverge greatly from the lithostatic stress at this depth due to the elastic distortion of rock from slip depending on the geometry of the fault. In addition, such a shallow depth is unexpected based on the occurrence of large stratigraphic offsets at this depth (Faulds and Garside, 2003; Lutz et al.,

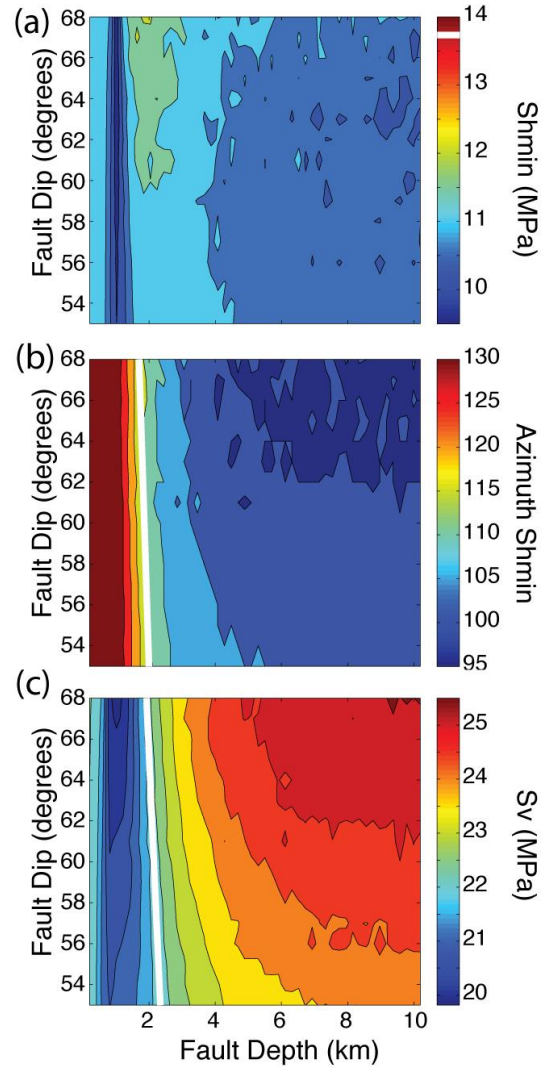


Figure 3: Plots of fault dip and depth parameter space. (a) S_{hmin} is best fit to DP 27-15 at 2 km fault depth and 71° but does not reach observed level shown as white line on color ramp. (b) Observed azimuth S_{hmin} is reached at this depth, as is (c) S_v assumed from weight of overlying rock.

2009; pers. comm. J. Faulds, Nov. 2011), which requires a much deeper lower termination to the actual fault. Although the fault model causes large rotations of stresses from the presence of the traction free surface, the fault geometry that produces a best fit to the observed stress state in the well of 71° dip and depth-extent of 2000 m will be used in the models for the rest of this study.

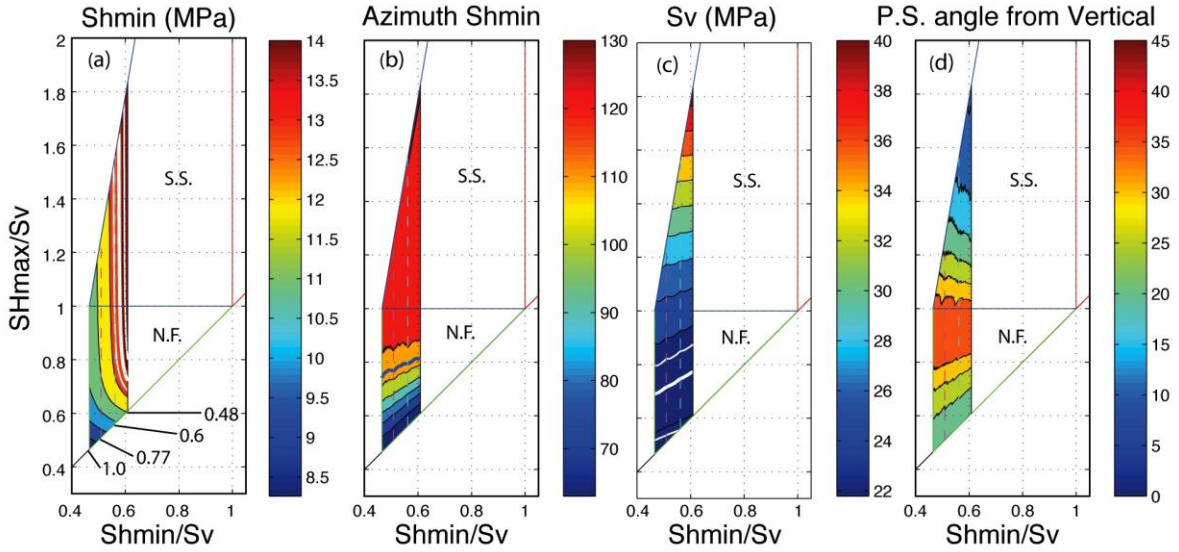


Figure 4: Stress polygons define the range of stress states that can be supported by the frictional strength of the crust. In these figures, the remote S_{hmin}^{remote} and S_{Hmax}^{remote} magnitudes are plotted normalized to S_v . The local conditions at the site of the mini-hydraulic fracturing test are contoured for (a) S_{hmin}^{loc} , (b) Azimuth^{loc}, and (c) S_v^{loc} .

(2) Stress Tensor Sensitivity Study

We investigated the sensitivity of the borehole observation and deformation around the fault to uncertainty in the remote stress tensor by modeling remote stress states that systematically sampled the range from the observed stress state to the most extreme ranges of S_{hmin} and S_{Hmax} allowed by the frictional strength of the crust (e.g., Townend and Zoback, 2002), which is here taken to be a coefficient of 1.0 as a maximum value consistent with Byerlee friction (Byerlee, 1978). Thus S_{hmin} at the depth of the mini-hydraulic fracture might vary from the observed magnitude of ~ 0.61 of S_v to the frictional limit of ~ 0.46 of S_v (Equation 1).

The four values of S_{hmin}^{rem} used were derived from various coefficients of friction using the critically stressed frictional failure criterion for normal faults described above (Equation 1). The S_{hmin}^{rem} magnitudes correspond to friction values of 0.48 which reproduces the stress state observed in the well (Hickman and Davatzes, 2010), 0.6 and 1.0 which represents the Byerlee friction range for a variety of brittle rocks (Byerlee, 1978), and 0.77 which is the value obtained from triaxial compression testing of rock samples from Desert Peak (Lutz et al., 2010). The stress tensor was aligned perpendicular remote stress state derived from a friction coefficient of 0.6. However, as S_{Hmax}^{rem} approaches the magnitude of S_{hmin}^{rem} , lower friction coefficients reproduce the observed S_{hmin}^{loc} magnitude. The azimuth of S_{hmin}^{loc} is very sensitive to S_{Hmax}^{rem} throughout the normal faulting zone, and the

with the fault strike just as in the study of simple fault geometry described above. This configuration minimizes the potential influence of S_{Hmax}^{rem} on stress rotations, as S_{Hmax}^{rem} acts parallel to the flat-planar fault. In cases where S_{Hmax}^{rem} is not aligned with the strike of the fault we expect similar behavior but with slightly greater sensitivity to the effects of S_{Hmax}^{rem} magnitude. The resulting range of stress states define a polygon with axes of S_{hmin}^{rem} and S_{Hmax}^{rem} normalized to the remote vertical stress, whose outer limits are given by the highest friction coefficient, the principal stresses, and the fluid pressure. This approach allows a range of physically permissible stress states from the normal faulting to strike slip faulting stress regimes to be assessed.

At the location of the DP 27-15 mini-hydraulic fracturing test, the simulations show that local S_{hmin} (S_{hmin}^{loc}) has little sensitivity to remote S_{Hmax}^{rem} for a value greater than 0.7 of S_v , which includes the strike slip and a portion of the normal faulting zone of the stress polygons. However, as S_{Hmax}^{rem} approaches the magnitude of S_{hmin}^{rem} , the simulations become increasingly sensitive to the choice of S_{Hmax}^{rem} and S_{hmin}^{rem} (Figure 4a). The model that best reproduced the observed magnitude of S_{hmin}^{loc} in the well is the observed value was achieved for a remote S_{Hmax}/S_v ratio of 0.8 (Figure 4b). The observed value of S_v assumed from the weight of overlying rock was found near this ratio as well (Figure 4c). As the maximum differential stress increases into the strike slip regime, the difference between S_v and the weight

of overburden increases due to the greater elastic deformation from increased slip on the fault. In the normal faulting regime, characterized by smaller maximum differential stress, S_v remains approximately equivalent to the weight of overburden regardless of fault slip at the position of DP 27-15.

Given the criterion for the correlation between the vertical fractures in the well and the orientation of the principal stresses stated above in the simple geometry study, a suitable model should have a principal stress oriented within 12-15 degrees from the axis of the well. Therefore, the maximum or intermediate principal stress should be aligned in the vertical direction depending on whether or not we consider the normal or strike-slip faulting regime respectively. These two principal stresses show the maximum offset from vertical for the remote stress state that produced the observed S_{hmin} (Figure 4d). Although once again this criterion is not satisfied, the stress tensor found to be the best fit to the observed S_{hmin} magnitude and direction was used for the fault overlap study.

(3) Fault Overlap Sensitivity Study

In order to explore the impact of the complex geometry of the Rhyolite Ridge fault system on the local stress state, and thus on fracture potential, two planar faults were arranged to mimic the strike of the major elements of the Rhyolite Ridge fault to simulate both: (1) the potential for the segments to slip independently since there is a large bend in the current fault trace leading to large differences in the ratio of the shear and normal tractions resolved on the segments and (2) the different stages in the evolution of the fault system geometry (Figure 5).

Both fault segments are assigned a lower tip depth of ~2000 m with the northern fault segment dipping 71° and the southern segment dipping 82.5° since its strike is offset from the northern fault by 22°. The southern fault segments northern tip was adjusted within the range of 2 km of overlap to 2 km of underlap. Since the second fault extends at least ~10 km to the south (Figure 1), the length of the southern fault is 6000 m in order to approximate the faults length so that it minimizes the effect of the southern tip on the model while also minimizing computation time (Figure 6). The far field stress state used was derived from the stress sensitivity study, and the direction of the stresses was taken from fault and fracture slip data collected in the field (Faulds, 2003) which is assumed to cause fault/fracture formation in order to investigate possible modes of fault propagation across the relay.

Idealized Map View Geometry (Rhyolite Ridge Fault System)

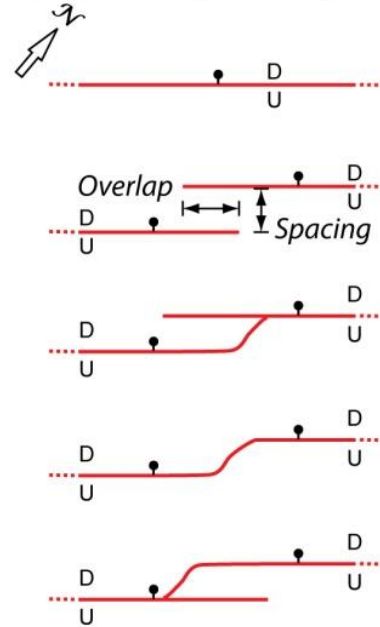


Figure 5: Simplified fault geometries, and modes of fault relay breach.

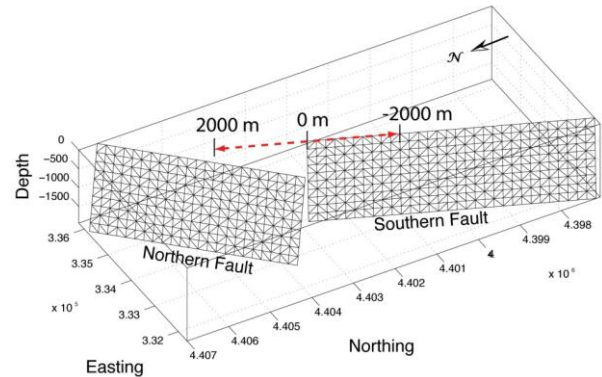


Figure 6: Model Setup for fault overlap at Rhyolite Ridge.

Figure 7a and b summarizes the magnitude and azimuth S_{hmin} at the observation point in well DP 27-15 for the series of simulations. Also shown are the simulated azimuths at well DP 23-1 at the observation depth of 1400-2800 m (Robertson-Tait et al., 2004) (figure 7c). The observed values in well DP 27-15 are achieved with roughly 600 meters of underlap and become increasingly less compressive with increasing overlap but do not approach tension, while the direction of S_{hmin} in well DP 23-1 did not show sensitivity to fault overlap retaining its correspondence to the input azimuth. Thus the pattern of slip among the segments can have a significant influence on the local stress state. In the simulated extreme case of a complete stress drop, the

local stress state observed at 27-15 characterized by relatively low differential stress can be reproduced from significantly larger far field differential stresses in the surrounding crust.

The potential for fracture formation or slip is assessed from maps and cross-sections of contoured stress parameters. Example contour maps derived from the local stress states due to the mechanical interaction of faults are shown for roughly 600 meters of underlap (Figure 8) and 600 meters of overlap (figure 9) in map view and cross section, with the cross section placed perpendicular to the average direction of the

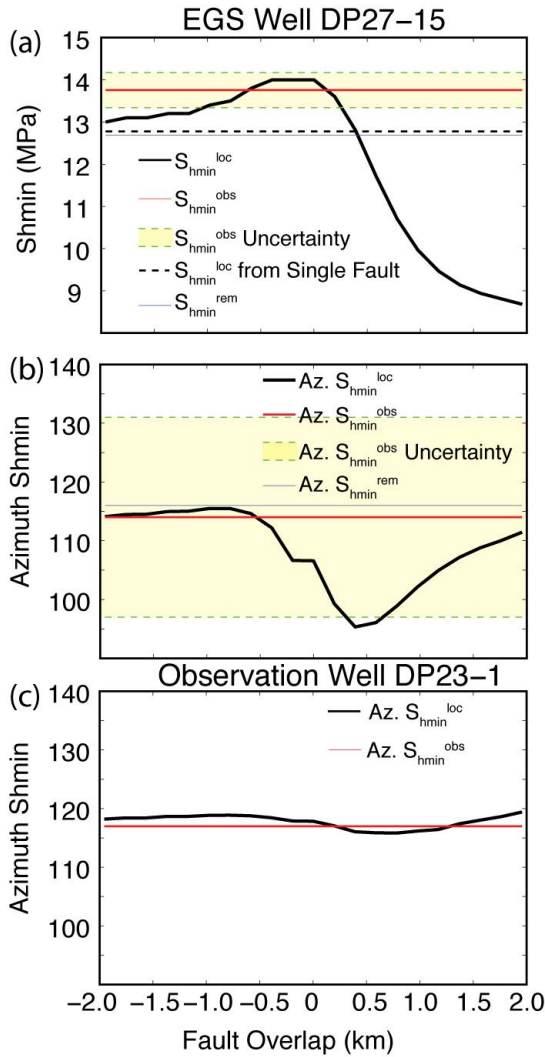


Figure 7: Results of fault overlap study. (a) S_{hmin}^{loc} plotted for fault over/underlap. Observed S_{hmin} in DP 27-15 found at ~600 m of fault underlap. (b) Azimuth S_{hmin}^{loc} faound there as well but nearly all models are within the uncertainty range. (c) Azimuth S_{hmin} for DP 23-1.

two fault strikes and between the two fault tips that are adjacent to each other in order to show the location of maximum fault interaction. Also shown

on the maps are the locations of a production well, two injection wells, and the location of the EGS well DP 27-15. Plots (a) and (b) in both Figures 8 and 9 show the value of S_{hmin} , as well as vectors perpendicular to the least compressive principal stress to show the strike of potential tensile fractures. Maps (c) and (d) from both Figures 8 and 9 show the Maximum Coulomb Shear Stress (S_c) on optimally oriented potential fracture surface as a proxy for fracture density (as per Maerten et al., 2002; Childs et al., 1995), with vectors of S_{Hmax} which are parallel to the strike of conjugate fracture planes that would result from compressive failure:

$$S_c = \left(\frac{(\sigma'_1 - \sigma'_3)}{2} \sqrt{1 + \mu_i^2} \right) - \mu_i \left(\frac{(\sigma'_1 + \sigma'_3)}{2} \right) \quad \text{Eq. 2}$$

where σ_1 and σ_3 are the maximum and minimum principal stresses, and μ_i is the internal coefficient of friction, and is taken to be 0.6. These plots show a significant increase in fracture potential at the northern tip of the southern fault and the fracture potential directions for the two types of rock failure show similar trends to the fault segments that connect these two portions of the Rhyolite Ridge fault (Figure 1b).

As per the criterion for fracture orientation in the well being indicative of a near vertical principal stress, the presence of the second fault caused the maximum compressive principal stress to be almost exactly vertical in the observation well for every model. This implies that the interaction between the two fault segments plays a critical role in causing the local stress state in the fault system, as well as the formation of a damage zone within the relay.

(4) Breached Relay Models

The mapped geometry of the Rhyolite Ridge fault contains several segments that connect the more extensive Northern and Southern Segments across the open relay modeled in Figures 8 and 9. The most prominent three segments were modeled to ascertain their impact on the local stress state in the relay. These can be interpreted from the abutting relationships to represent: 1) propagation of the southern fault with a curve to join with the northern fault, 2) propagation of the northern fault and a truncated intersection with the southern fault, and 3) propagation of the southern fault segment following the general direction of its strike with bends representing locations where secondary faults breach the relay at several locations (Figure 1b). The magnitude and direction of remote S_{hmin} corresponds with the measurements in well DP 27-15 (Table 1) in order to show the effect of the present

stress state on the mapped fault traces, with the ratio of SH_{max} to S_v derived from the stress sensitivity study. The first and second fault traces modeled (1 in Figure 10a, and 2 in Figure 10d) show areas of enhanced dilational failure potential due to a reduced compression of Sh_{min} in the area of production associated with their right turning bends, and the right turning bends in this third fault trace create locations of enhanced compression where the secondary faulting of the relay occurs (Figure 10 g & h).

DISCUSSION

These models provide a tool for assessing how uncertainties in data sets translate to uncertainties in conceptual models, for instance how a fault geometry or stress state impacts the prediction of fracture density or the position of a geothermal resource.

Although the single fault model produced very large stress rotations that were not observed in the wells, the overlapping relay caused by the second fault served to minimize the vertical stress rotations, while concentrating stresses and causing potential fracture orientations that resemble the relay faulting pattern and promote connectivity between injection, production, and EGS wells. The role of the three faults within the relay modeled at Rhyolite Ridge cause the stress concentrations to be reduced and offset from the unbreached relay model, but focus stress concentrations within the production area. Further structural assessment of Rhyolite Ridge should include modeling the combined effects of all three fault traces together, as the points where they intersect most likely create areas of stress concentrations as well.

Limitations of the model and Future Development

Although this study provides some insight into the structural mechanisms related to faults and fractures, there is still potential for further exploration of other fault parameters that could greatly affect the model result. The fault geometries in this study have no roughness in the down-dip direction, and the roughness in the horizontal direction was taken from the projected fault trace into the ground. Although fault roughness has been shown to be reduced in the dominant slip direction (Power et al., 1987, 1988; Sagy et al., 2006) modeling faults in this way is not necessarily accurate. In addition, the volume experiencing stress perturbation is proportional to the length of the source roughness. Thus, the large-scale patterns in stress perturbation relevant to this study will generally be independent of the roughness at smaller

length scales. However, this behavior might change in the presence of frictional faults that can support residual shear tractions (Parsons 2002; Kaven et al., in press). For simple fault geometries, varying the shear stress drop primarily reduces the volume experiencing large stress magnitude changes and principal stress rotations. However, for geometries more consistent with the complexity of the mapped trace of the Rhyolite Ridge fault, the inclusion of residual frictional strength changes the location of some of the volumes experiencing locally enhanced Coulomb Shear stress indicative of fracture formation or reactivation. In addition, inclusion of friction will allow us to assess the dilation potential of the Rhyolite Ridge system itself, and by allowing opening, an assessment of not only off-fault fracture potential, but whether the fault is a primary connection to hot fluids at depth.

Further development of this fault model will include a study of fault roughness, friction and how stress states near the fault are further perturbed due to fault opening and stress concentrations at point contacts. Other aspects of fault geometry that can be modeled are curvature at the fault tips with depth and listric fault geometry commonly attributed to Basin and Range normal faults (Stein, 1985). Friction can be modeled using existing solutions including the (1) iterative solver incorporated into Poly3D by IGEOS, and (2) a linear complementarity friction solver (Kaven et al., in press).

This exploration of uncertainty will form the basis for developing statistical measures of the probability and validity of reservoir models.

ACKNOWLEDGEMENTS

We would like to thank James Faulds for sharing detailed maps and geologic insights concerning the structure of the Rhyolite Ridge fault as well as useful discussions with Inga Moeck. Stephen Peterson digitized the fault traces. We thank J. Ole Kaven for reviewing the Manuscript. This research was funded by ORMAT Nevada.

REFERENCES

- Barton, C. A., M. D. Zoback, and D. Moos (1995), Fluid flow along potentially active faults in crystalline rock, *Geology*, 23, 683–686.
- Barton, C., Hickman, S., Morin, R., Zoback, M.D., Benoit, R. (1998). Reservoir-scale Fracture Permeability in the Dixie Valley, Nevada, Geothermal Field. Edited by Holt, R.M. *Rock Mechanics in Petroleum Engineering*, v. 2:

- Richardson, TX, Society of Petroleum Engineers, v. 2 p. 315-322.
- Benoit, D. and Blackwell, D.D., 2006, Exploration of the Upper Hot Creek Ranch, Nye County, Nevada geothermal system: Geothermal Resources Council Transactions v. 30.
- Bruhn, R. L., Parry, W. T., Yonkee, W. A., and Thompson, T. (1994). Fracturing and hydrothermal alteration in normal fault zones: PAGEOPH, v. 142, p. 609–644.
- Byerlee, J.D. (1978). Friction of Rocks. Pure and Applied Geophysics v. 116 n. 4-5 p. 615-626.
- Caine, J.S., J.P. Evans, and C.B. Forster (1996) Fault zone architecture and permeability structure, Geology, v1025-1028.
- Crider, J.G., Pollard, D.D. (1998) Fault linkage: Three-dimensional mechanical interaction between echelon normal faults. Journal of Geophysical Research v. 103 n. B10 p. 24,373-24,391.
- Crouch, S. L. Starfield, A. M. (1983). Boundary element methods in solid mechanics: With applications in rock mechanics and geological engineering: London, Unwin Hyman, 322 p.
- Coolbaugh, M.F., Sladek, C., Faulds, J.E., Zehner, R.E., Oppliger, G.L. (2007). Use of rapid temperature measurements at a 2-meter depth to augment deeper temperature gradient drilling. PROCEEDINGS: Thirty-Second Workshop on Geothermal Reservoir Engineering, Stanford University, Stanford, California, January 22-24, 2007.
- Curewitz, D., Karson, J.A. (1997). Structural Settings of Hydrothermal Outflow: Fracture Permeability Maintained by Fault Propagation and Interaction. Journal of Volcanology and Geothermal Research v. 79 p. 149-168.
- Davatzes, N.C., Hickman, S.H. (2009). Fractures, Stress and Fluid Flow Prior to Stimulation of Well 27-15, Desert Peak, Nevada, EGS Project. PROCEEDINGS: Thirty-Fourth Workshop on Geothermal Reservoir Engineering, Stanford University, Stanford, California, February 9-11, 2009.
- Davatzes, N.C., Eichhubl, P., Aydin, A. (2005). Structural Evolution of Fault Zones in Sandstone by Multiple Deformation Mechanisms: Moab Fault, Southeast Utah. Geologic Society of America Bulletin; January/February 2005; v. 117 p. 135-148.
- Eichhubl, P., Davatzes, N.C., Becker, S.P. (2009). Structural and Diagenetic Control of Fluid Migration and Cementation along the Moab Fault, Utah. American Association of Petroleum Geologists Bulletin, v. 93 n. 5 p. 653-681.
- Fairley, J.P., Hinds, J.J. (2004) Field observation of fluid circulation patterns in a normal fault system. Geophysical Research Letters, v. 31, L19502, doi:10.1029/2004GL020812.
- Faulds, J.E., Coolbaugh, M.F., Benoit, D., Oppliger, G. (2010). GRC Transactions, v. 34.
- Faulds, J.E., Coolbaugh, M., Blewitt, G., Henry, C.D. (2004), Why is Nevada in Hot Water? Structural Controls and Tectonic Model of Geothermal Systems in the Northwestern Great Basin. Geothermal Resources Council Annual Meeting, Aug.-Sept. 2004, Palm Springs, CA.
- Faulds, J.E., Garside, L.J. (2003). Preliminary Geologic Map of the Desert Peak – Brady Geothermal Fields, Churchill County, Nevada. Nevada Bureau of Mines and Geology Open-File Report 03-27.
- Faulds, J.E., Garside, L.J., Oppliger, G.L. (2003). Structural Analysis of the Desert Peak-Brady Geothermal Fields, Northwestern Nevada: Implications for Understanding Linkages between Northeast-Trending Structures and Geothermal Reservoirs in the Humboldt Structural Zone. Geothermal Resources Council Transactions, v. 27 p. 859-864.
- Hickman, S.H., Davatzes, N.C. (2010). In-Situ Stress and Fracture Characterization for Planning of an EGS Stimulation in the Desert Peak Geothermal Field, Nevada. PROCEEDINGS: Thirty-Fifth Workshop on Geothermal Reservoir Engineering, Stanford University, Stanford, California, February 1-3, 2010.
- Hickman, S., Zoback, M.D., Benoit, R. (1998), Tectonic controls on fault-zone permeability in a geothermal reservoir at Dixie Valley, Nevada, in Rock Mechanics in Petroleum Engineering, v. 1, R. M. Holt et al. (eds.), Soc. Petroleum Eng., Richardson, TX., p. 79-86.
- Jaeger, J.C., Cook, N.G.W. (1979) Fundamentals of Rock Mechanics. Chapman and Hall, London.
- Kaven, J.O., et al. (2010) Mechanical analysis of fault slip data: Implications for paleostress analysis, Journal of Structural Geology, doi:10.1016/j.jsg.2010.12.004
- Kratt, C., Calvin, W., Coolbaugh, M. (2006). Geothermal Exploration with Hymap Hyperspatial Data at Brady-Desert Peak, Nevada. Remote Sensing of Environment v. 104 p. 313-324.

- Lutz, S.J., Hickman, S., Davatzes, N., Zemach, E., Drakos, P., Robertson-Tait, A. (2010). Rock Mechanical Testing and Petrologic Analysis in Support of Well Stimulation Activities at the Desert Peak Geothermal Field, Nevada. PROCEEDINGS: Thirty-Fifth Workshop on Geothermal Reservoir Engineering, Stanford University, Stanford, California, February 1-3, 2010.
- Lutz, S.J., Moore, J.N., Jones, C.G., Suemnicht, G.A., Robertson-Tait, A. (2009). Geological and Structural Relationships in the Desert Peak Geothermal System, Nevada: Implications for EGS Development. PROCEEDINGS: Thirty-Fourth Workshop on Geothermal Reservoir Engineering, Stanford University, Stanford, California, February 9-11, 2009.
- Maerten, L., Gillespie, P., Pollard, D.D. (2002). Effects of Local Stress Perturbation on Secondary Fault Development. *Journal of Structural Geology* v. 24 p. 145-153.
- Maerten, L., Willemsse, M.J., Pollard, D.D., Rawnsley, K. (1999). Slip distributions on intersecting normal faults. *Journal of Structural Geology* v. 21 p. 259-271.
- Martel, S.J., Pollard, D.D., Segall, P. (1998). Development of simple fault zones in granitic rock, Mount Abbot quadrangle, Sierra Nevada: *Journal of Geophysical Research*, v. 94 p. 1451-1465.
- Micklethwaite, S., Sheldon, H.A., Baker, T. (2010). Active Fault and Shear Processes and their Implications for Mineral Deposit Formation and Discovery. *Journal of Structural Geology* v. 32 p. 151-165.
- Muller, J. R., and A. Aydin (2005). Using mechanical modeling to constrain fault geometries proposed for the northern Marmara Sea, *J. Geophys. Res.*, 110, B03407, doi:10.1029/2004JB003226.
- Myers, R.D., and Aydin, A. (2004). The evolution of faults formed by shearing across joint zones in sandstone. *Journal of Structural Geology*, v. 26 p. 947-966, doi:10.1016/J.JSG.2003.07.008
- Parsons, T. (2002). Nearly frictionless faulting by unclamping in long-term interaction models, *Geology*, v. 30, p. 1063–1066.
- Peška, P., Zoback, M.D. (1995). Compressive and tensile failure of inclined well bores and determination of in situ stress and rock strength. *Journal of Geophysical Research* v. 100 n. B7 p. 12,791-12,811.
- Power, W. L., Tullis, T. E., Brown, S. R., Boitnott, G. N., and Scholz, C. H., 1987, Roughness of natural fault surfaces, *Geophys. Res. Lett.*, 14, 29-32.
- Power, W. L., Tullis, T. E., and Weeks, J. D., 1988, Roughness and wear during brittle faulting, *J. Geophys. Res.*, 93, 15268-15278.
- Robertson-Tait, A., Lutz, S.J., Sheridan, J., Morris, C.L. (2004). Selection of an Interval for Massive Hydraulic Stimulation in Well DP 23-1, Desert Peak East EGS Project, Nevada. . PROCEEDINGS: Twenty-Ninth Workshop on Geothermal Reservoir Engineering, Stanford University, Stanford, California, January 26-28, 2004.
- Sagy, A., E.E. Brodsky, and G.J. Axen (2006). Evolution of fault surface roughness with slip, *Geology*, v. 35, p. 283-286.
- Thomas, A.L. (1993). Poly3D: a three-dimensional, polygonal-element, displacement discontinuity boundary element computer program with applications to fractures, faults, and cavities in the Earth's crust. M.S. thesis, Stanford University, California.
- Townend, J., and M. D. Zoback (2000). How faulting keeps the crust strong, *Geology*, 28, 399– 402.
- Smith, L., C. Forster, and J. Evans (1990), Interaction of fault zones, fluid flow, and heat transfer at the basin scale, in *Hydrogeology of Low Permeability Environments: From a Special Symposium at the 28th International Geological Congress, Washington, D.C., U.S.A., July 9 – 19, 1989*, Hydrogeology, vol. 2, edited by S. P. Neuman and I. Neretnieks, pp. 41 – 67, Verlag Heinz Heise, Hanover, Germany.
- Zemach, E., Drakos, P., Robertson-Tait, A. (2009). Feasibility Evaluation of an “in-field” EGS project at Desert Peak, Nevada. *Geothermal Resources Council Transaction*, v. 33, p. 285-295.
- Zoback, M.D. (2007). *Reservoir Geomechanics*. Cambridge University Press, Cambridge U.K.

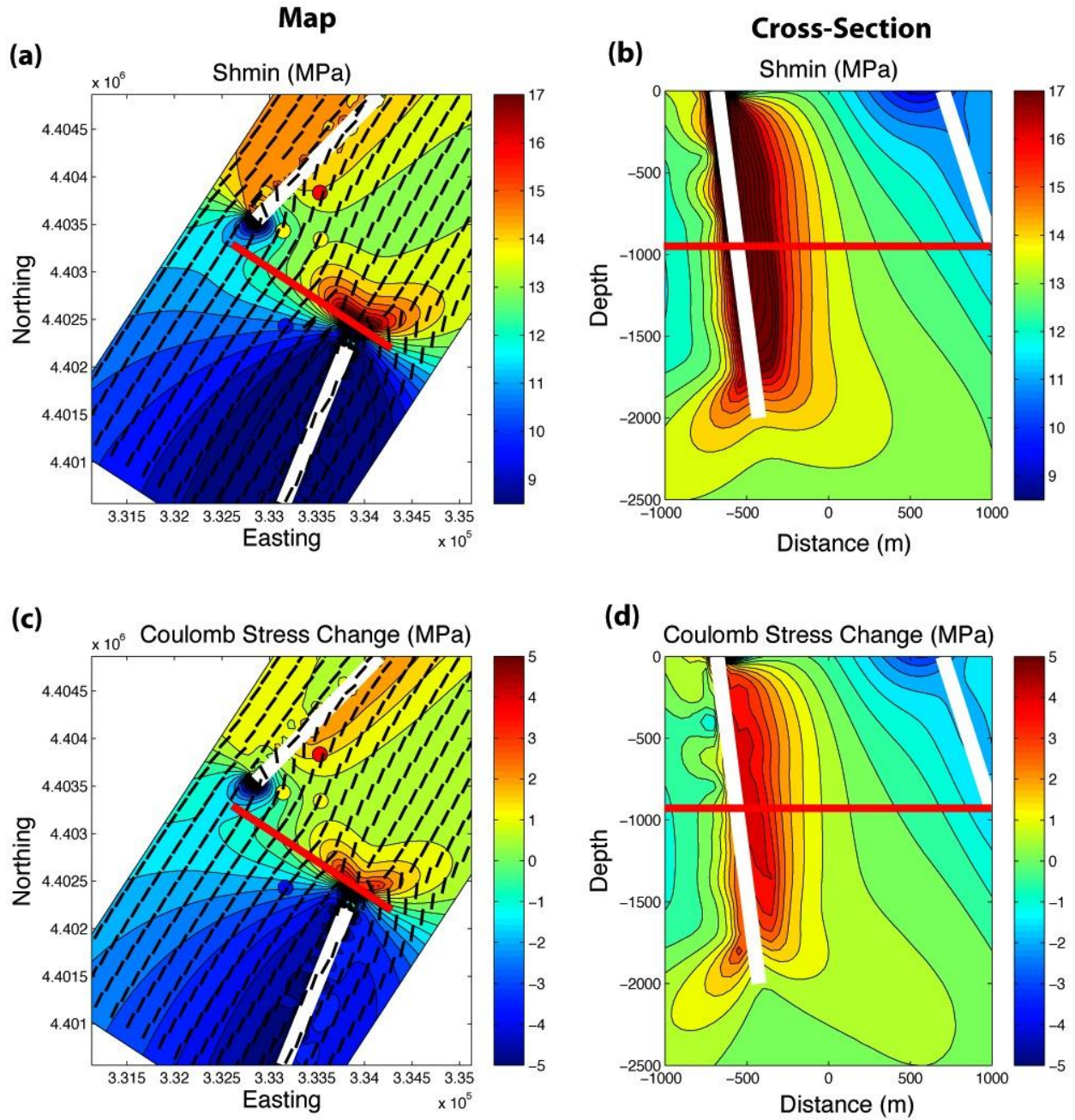


Figure 8: Underlapping faults. Map views (a & c) showing injection wells (yellow) production wells (blue) and EGS well DP27-15 (red) as well as location of cross section with red line. Cross sections (b & d) showing modeling/observation depth for stimulation interval in EGS well DP27-15.

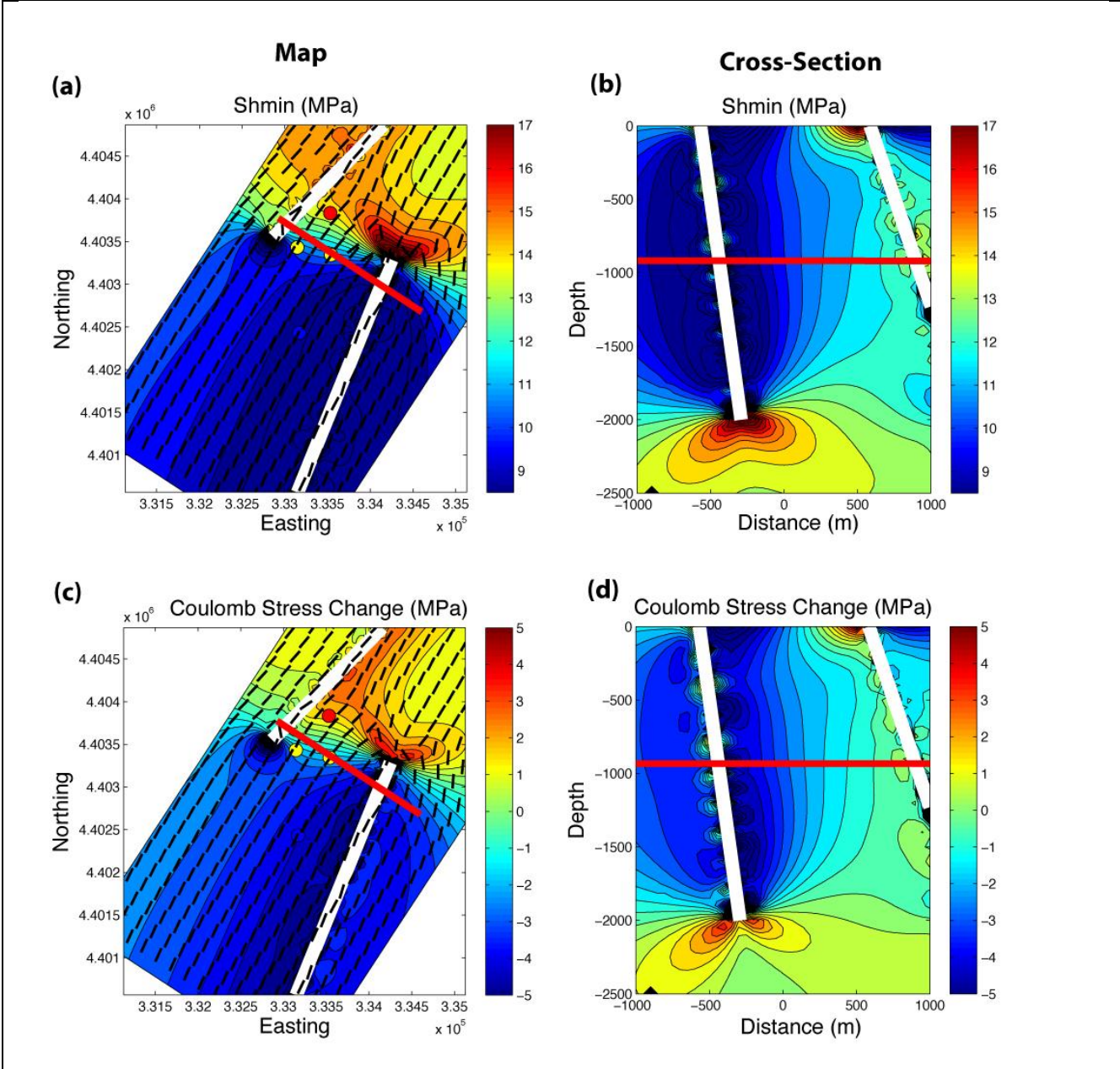


Figure 9: Overlapping faults. Map views (a & c) showing injection wells (yellow) production wells (blue) and EGS well DP27-15 (red) as well as location of cross section with red line. Cross sections (b & d) showing modeling/observation depth for stimulation interval in EGS well DP27-15.

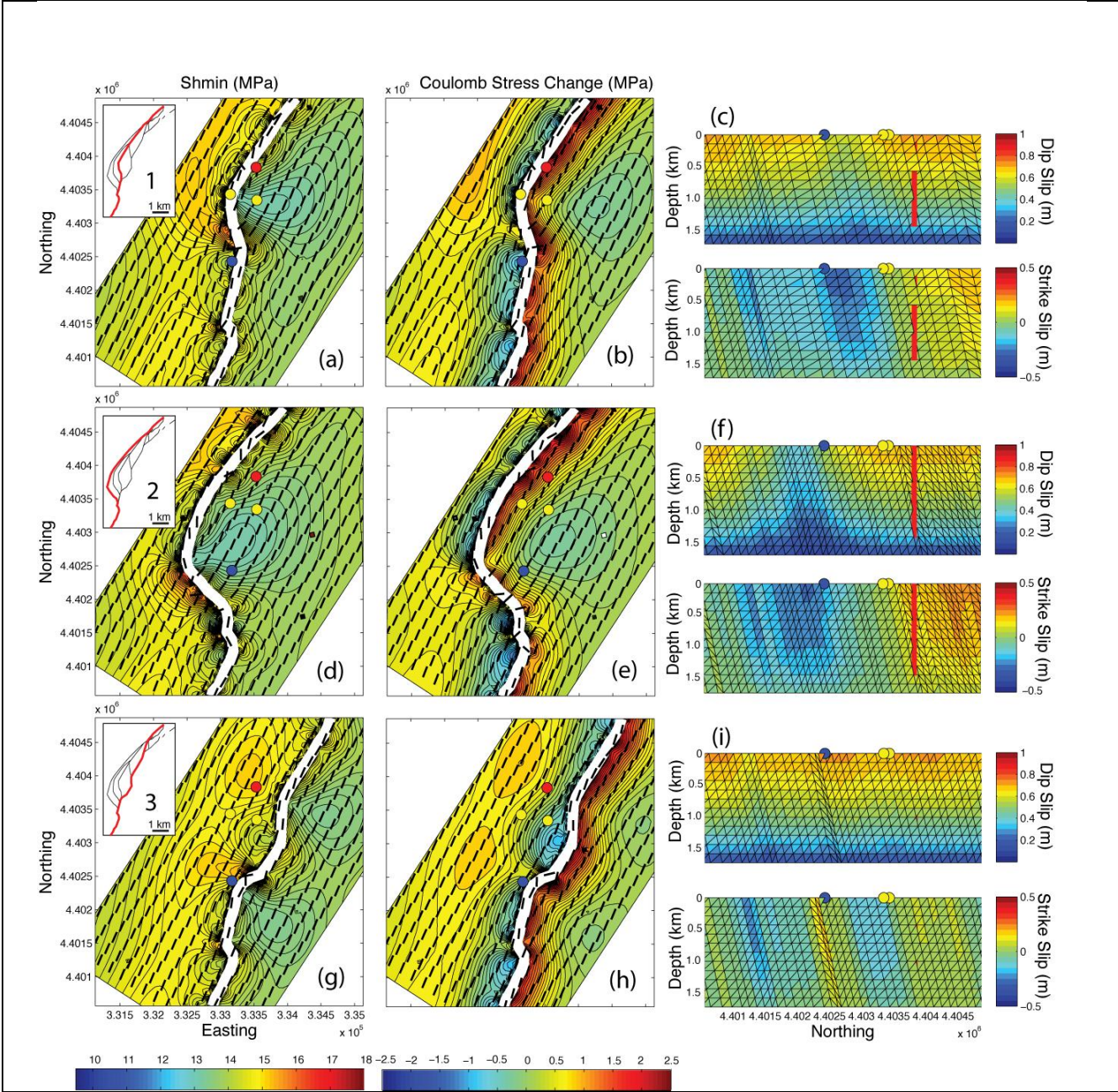


Figure 10: Three faults modeled that breach the relay at Desert Peak. Cross sections showing modeled slip distribution facing due west. The figures show injection wells (yellow) production wells (blue) and EGS well DP27-15 (red).

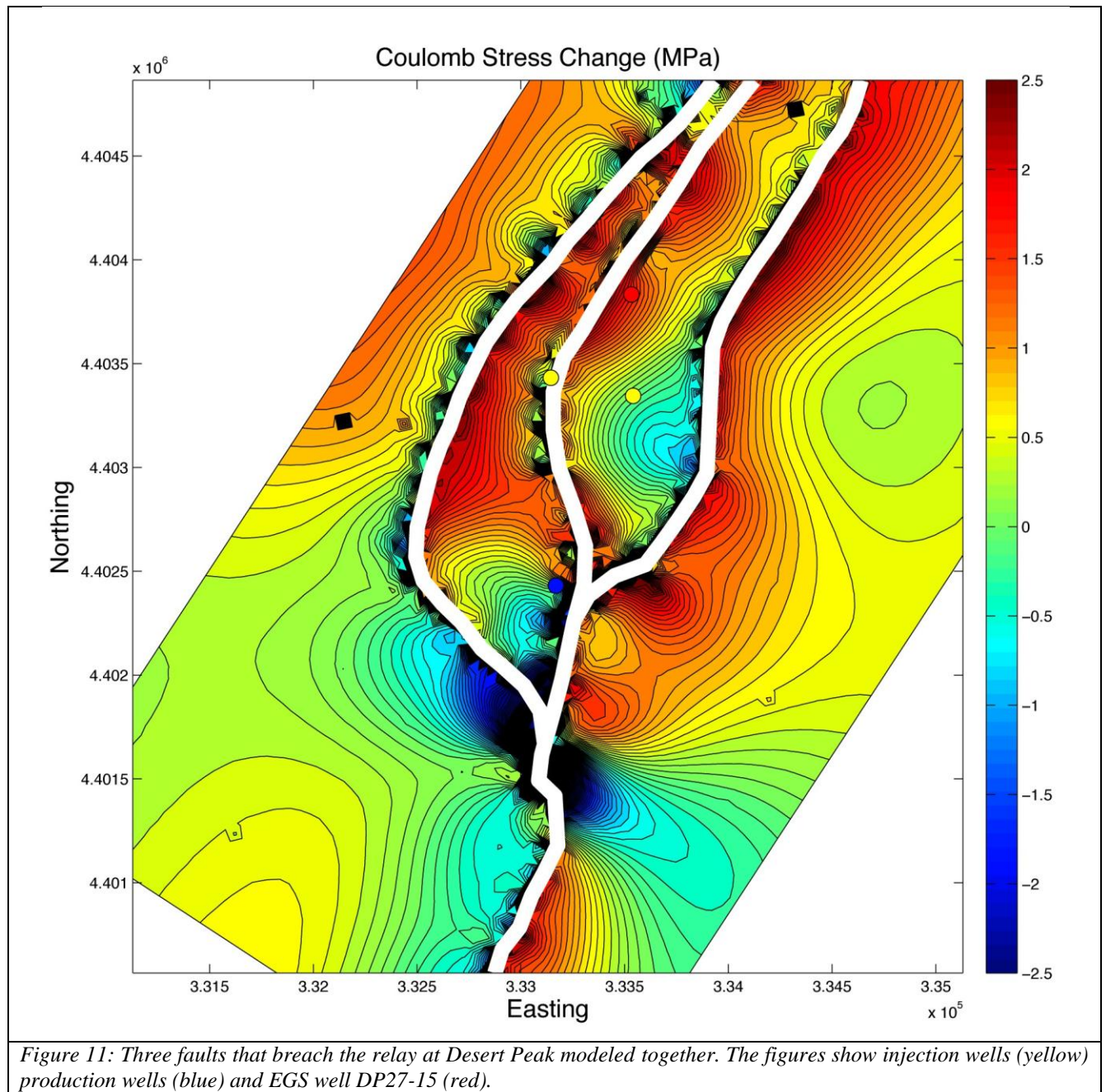


Figure 11: Three faults that breach the relay at Desert Peak modeled together. The figures show injection wells (yellow) production wells (blue) and EGS well DP27-15 (red).